PONTIFICIA UNIVERSIDAD CATOLICA DE CHILE
SCHOOL OF ENGINEERING

SCALE-INVARIANT DEEP LEARNING APPROACH FOR QSM RECONSTRUCTION: SI-QSM

JOSE MANUEL LARRAIN

Thesis submitted to the Office of Graduate Studies
in partial fulfillment of the requirements for the Degree of
Master of Science in Engineering

Advisors:
CRISTIÁN TEJOS
HANS LÖBEL

Santiago de Chile, May 2022

PONTIFICIA UNIVERSIDAD CATOLICA DE CHILE
SCHOOL OF ENGINEERING

SCALE-INVARIANT DEEP LEARNING APPROACH FOR QSM RECONSTRUCTION: SI-QSM

JOSE MANUEL LARRAIN

Members of the Committee:
CRISTIÁN TEJOS
HANS LÖBEL
RODRIGO CÁDIZ
CARLOS MILOVIC
IGNACIO VARGAS

Thesis submitted to the Office of Research and Graduate Studies
in partial fulfillment of the requirements for the degree of
Master of Science in Engineering

Santiago de Chile, May 2022

To my family and friends

PREFACE

This thesis document presents the works performed by José Manuel Larraín De Andraca during his Master of Science in Engineering. The main work (”Scale-invariant Deep Learning approach for QSM reconstruction: SI-QSM”) of this thesis was submitted to the journal NeuroImage in April 2022 (Query NIMG-22-804) and waiting for approval.

ACKNOWLEDGEMENTS

First I want to thank my advisors Cristián Tejos and Hans Löbel, who opened the doors to the world of research. I greatly appreciate how you have believed in me the opportunities you have given me, the teachings you have transmitted to me, and your supervision and attention.

Special thanks to Carlos Milovic and Mathias Lambert, for their friendship, and trust, for sharing their knowledge and ideas with me.

I thank my family and friends. For walking next to me on the road to finish my degree and encouragement in difficult moments.

TABLE OF CONTENTS

PREFACE iv

ACKNOWLEDGEMENTS v

LIST OF FIGURES vii

LIST OF TABLES viii

ABSTRACT ix

RESUMEN x

1. INTRODUCTION 1

2. Methods 5

    2.0.1. Network Architecture 5

    2.0.2. Data generation 7

    2.0.3. Model training 9

    2.0.4. Experiments 10

3. Results 13

    3.0.1. Scale invariance 13

    3.0.2. QSM Reconstruction Challenge data 14

    3.0.3. In vivo data 16

4. Discussion 19

5. Conclusions 22

REFERENCES 23

LIST OF FIGURES

2.1 SI-QSM architecture. 6

2.2 Generated training data with inputs and expected outputs. 9

3.1 Comparison of CNN-based QSM reconstructions at different FOV scales. All susceptibility values are in ppm. 14

3.2 QSM reconstructions (in ppm) obtained by different methods using the RC2 data. 15

3.3 Difference maps between the ground truth and the compared reconstruction approaches. All results are in ppm. 15

3.4 QSM reconstructions (in ppm) of a healthy volunteer. 17

3.5 QSM reconstructions (in ppm) of a subject with a calcification. 18

3.6 QSM reconstructions (in ppm) of a subject with a calcification. Magnified view of a ROI around the calcification. 18

LIST OF TABLES

3.1 RMSE results for the CNN-based QSM reconstruction method in ppm. 13

3.2 Metric scores obtained by different reconstruction methods using the RC2 data. 16

ABSTRACT

Quantitative susceptibility mapping (QSM) is an MRI-based technique that allows the quantification of the magnetic susceptibility of tissues. This technique has emerge as a potential biomarker for several brain diseases. QSM reconstruction process involves solving an ill-posed inverse problem. Iterative approaches might solve that problem, but at the expense of tedious and time-consuming heuristic schemes to set weighting parameters. Deep learning approaches have emerged as alternative solutions. Despite of their relative success, these approaches still present some problems when there is a mismatch in spatial scale between the training datasets and the reconstructed susceptibility maps.

We propose an alternative deep learning QSM approach that incorporates novel training and architecture features. Our training datasets are based on analytical models and our loss function balances L1-norm, L2-norm and a total variation regularization. Our U-net-based architecture combines residual layers and different types of kernels with different sizes.

We trained our network at one particular spatial scale and we tested it with in silico and real data of different spatial scales. We compared our performance against state of the art iterative and deep learning QSM techniques. Our network can be trained at one particular spatial scale and obtain accurate QSM reconstructions at different scales, without producing blurred structures, biased susceptibilities and with good control over noise, streaking or similar artifacts. Furthermore, our algorithm outperformed standard deep learning alternative and produced QSM reconstructions of similar quality as those obtained by state of the art iterative solvers, but it is substantially faster and it does not use any heuristic for tuning weighting parameters.

Keywords: Magnetic Resonance Imaging, Artificial Intelligence, Dipole inversion, Inverse problems, Quantitative susceptibility mapping.

RESUMEN

Mapas cuantitativos de susceptibilidad (QSM) es una técnica basada en resonancia magnética que permite cuantificar la susceptibilidad magnética de los tejidos. Esta técnica ha surgido como un biomarcador potencial para varias enfermedades neurológicas. El proceso de reconstrucción QSM implica la resolución de un problema inverso mal comportado. Actualmente las soluciones iterativas resuelven el problema utilizando heurísticas difíciles de implementar y con alto tiempo de cómputo. Métodos aplicando inteligencia artificial han surgido como soluciones alternativas. Pese a su éxito, estos métodos siguen presentando problemas cuando hay un desajuste en la escala espacial entre los conjuntos de datos de entrenamiento y los mapas de susceptibilidad a reconstruir.

En este trabajo se propone la alternativa de inteligencia artificial SI-QSM, que incorpora en su algoritmo el estado del arte de entrenamiento y arquitectura. Los datos de entrenamiento se basan en el modelo analítico y la función de pérdida equilibra la norma L1, la norma L2 y una regularización de variación total. La arquitectura está basada en U-net con capas residuales y kernels con diferentes tamaños.

SI-QSM fue entrenado a una escala espacial y probado con simulaciones y datos in-vivo de diferentes escalas espaciales. Se comparó las reconstrucciones de SI-QSM con los estados del arte iterativos e inteligencia artificial. Concluyendo que SI-QSM puede inferir QSM precisas a diferentes escalas, sin producir estructuras borrosas, susceptibilidades sesgadas y con un buen control del ruido o artefactos. Además, SI-QSM superó las otras alternativas de inteligencia artificial y produjo reconstrucciones de calidad similar a las obtenidas por los soluciones iterativas, pero es sustancialmente más rápido y sin necesidad de utilizar ninguna heurística para ajustar los parámetros.

Palabras Claves: Imágenes resonancia magnética, Inteligencia artificial, Inversión dipolo, Problema inverso, Mapas de susceptibilidad magnética.

1. INTRODUCTION

Quantitative susceptibility mapping (QSM) is a Magnetic Resonance Imaging (MRI)-based technique used to determine the magnetic susceptibility of tissues, given the phase of a complex-valued gradient recalled echo (GRE) acquisition (Wang & Liu, 2015; E. M. Haacke et al., 2015). The magnetic susceptibility can be defined as the ratio between the magnetization of an element and the applied magnetic field (E. M. Haacke et al., 2015; Duyn et al., 2007) and is directly related to the tissue chemical composition. Diamagnetic tissues create a magnetization field that opposes the main magnetic field, whereas paramagnetic tissues present a magnetization in the same direction as the main magnetic field. This enables QSM to differentiate between, for example, (diamagnetic) calcium and (paramagnetic) iron depositions (E. M. Haacke et al., 2015). This technique has been used to study the brain, including physiological processes (e.g., oxygenation (M. Haacke, Tang, Neelavalli, & Cheng, 2010)), pathological events (e.g., microbleeds (T. Liu et al., 2012)), and neurodegenerative diseases (e.g., Alzheimer's (Acosta-Cabronero et al., 2013), Parkinson's (Acosta-Cabronero et al., 2017; Langkammer et al., 2016), Multiple Sclerosis (Zhang et al., 2016)).

QSM images are typically obtained after solving 3 consecutive stages: unwrapping, background field removal and dipole inversion. The continuous total magnetization field is proportional to the phase of the acquired GRE signal. Due to the periodic nature of this phase signal, the resulting measurements have 2π-jumps which are eliminated by phase unwrapping methods (Robinson et al., 2017). The background field removal stage aims at eliminating the magnetic field contributions produced by objects outside the regions of interest (ROI) and field inhomogeneities (Schweser, Robinson, de Rochefort, Li, & Bredies, 2017). Finally, the dipole inversion stage estimates the magnetic susceptibility of the examined tissues from the local field map obtained in the previous stage by solving an ill-posed inverse problem.

Since typical tissue susceptibilities are small (in the order of parts-per-million, or ppm), it can be assumed that a tissue is made of a distribution of independent susceptibility sources that do not interact with each other. This way, the local field map can be modeled as the convolution between a magnetic dipole kernel and the susceptibility distribution. In QSM, this model is known as the source-to-field or forward problem. Estimating the susceptibility distribution is, in essence, a deconvolution (or inverse) problem. These kinds of problems are commonly solved in the frequency domain, since spatial convolutions are simple voxel-wise multiplications of the Fourier transform of the arguments. However, the Fourier transform of the dipole kernel has zero-valued coefficients along a double conical surface (known as the *magic cone*). Therefore, the deconvolution cannot be solved by direct division in the frequency domain (Salomir, Senneville, & Moonen, 2003; J. Marques & Bowtell, 2005).

Approaches based on truncated divisions (Shmueli et al., 2009; Wharton & Bowtell, 2010) (i.e., replacing zeros by a small constant before the direct division) tend to amplify noise effects, generating streaking artifacts, i.e., high intensity lines in the same orientation as that of the surface of the magic cone. To deal with artifacts related to noise and errors propagated from previous stages, most of the current QSM reconstruction algorithms are based on iterative methods (Bilgic, Chatnuntawech, Langkammer, & Setsompop, 2015; Wharton, Schäfer, & Bowtell, 2010; T. Liu, Liu, et al., 2011). Such approaches formulate the reconstruction as the minimization of a functional, consisting typically of a data consistency term and a regularization term. The first term enforces the proposed solution and the measured local phase to be consistent with the forward problem, given a known noise distribution. The second term enforces prior knowledge regarding the solution (e.g., smoothness or sparsity in some domain). These two terms are balanced by a Lagrangian weight. Finding the right weight is not straightforward. This is normally done using some heuristic (e.g., L-curve (Hansen, 1992), or regional analysis in the Fourier domain (Milovic et al.,

2021)) that involves solving the optimization problem several times, each one with a different weight. Therefore, these iterative algorithms tend to be tedious and time-consuming.

Alternative data-driven QSM reconstruction methods have recently appeared using deep learning-based techniques (Yoon et al., 2018; Bollmann et al., 2019; Jung, Bollmann, & Lee, 2020; Gao et al., 2021). Most of these methods use convolutional neural networks (CNN), usually based on U-net-like architectures (Ronneberger, Fischer, & Brox, 2015). This kind of architecture facilitates reconstructing volumes that preserve morphological similarities. Generative adversarial networks (GAN)(Goodfellow et al., 2014) and other alternative architectures have been also implemented (Chen, Jakary, Avadiappan, Hess, & Lupo, 2020; Feng et al., 2021), being less popular than U-net-based solutions.

Compared with iterative methods, CNN-based reconstructions are faster and they do not need any heuristic to fine tune weighting parameters. However, CNN-based methods still present some challenges. Current reconstructions methods tend to be over-smoothed and their accuracy is deteriorated. CNN-methods tend to produce underestimated susceptibilities when the training data set and the actual reconstructed data significantly differ in their susceptibility ranges (Yoon et al., 2018; Oh, Bae, Ahn, Park, & Ye, 2020). Another important problem arises when the training data set and the actual reconstructed data differ in spatial scale or resolution (Chen et al., 2020; Oh et al., 2020), as reconstruction accuracy is greatly reduced. A standard approach to avoid such problem is to have the same spatial resolution in both, the training data (full-size images or sliding patches) and the actual reconstructions. However, this approach constrains significantly the applicability of the methods or alternatively, force to have a series of training data sets of different spatial resolutions.

In this work, we present a scale-invariant Deep Learning approach for QSM reconstruction (SI-QSM). Our network architecture combines residual layers, filters of different

sizes and training data based on analytic models to effectively reduce the problems generated by a scale mismatch between training and reconstructed data. Therefore, training at one particular spatial scale could be used to reconstruct accurately QSM maps from GRE data obtained at different scales. The source code of SI-QSM is available at `https://github.com/jnlarrain/ReconstrucNetwork`

2. METHODS

2.0.1. Network Architecture

Our proposed network architecture (Figure 2.1) is based on a 3D fully-convolutional residual U-net, with 1x1x1 convolutional layers used to reduce dimensions. To reduce the number of training weights and computational resources, we used a parallel layer paradigm with filters of different sizes as those introduced in the Inception Net architecture (Szegedy et al., 2014). As inputs, our model uses the local field map and a binary mask of the ROI, which are concatenated in two channels.

Due to the down-sampling and up-sampling steps, our network architecture allows reconstructing any image whose size is a factor of 16. For images of other sizes, this requirement needs to be fulfilled by zero-padding the data in a preprocessing step. Given that the local magnetization fields are typically masked and should decay quickly to zero outside the ROI, zero-padding acts as a reasonable boundary condition.

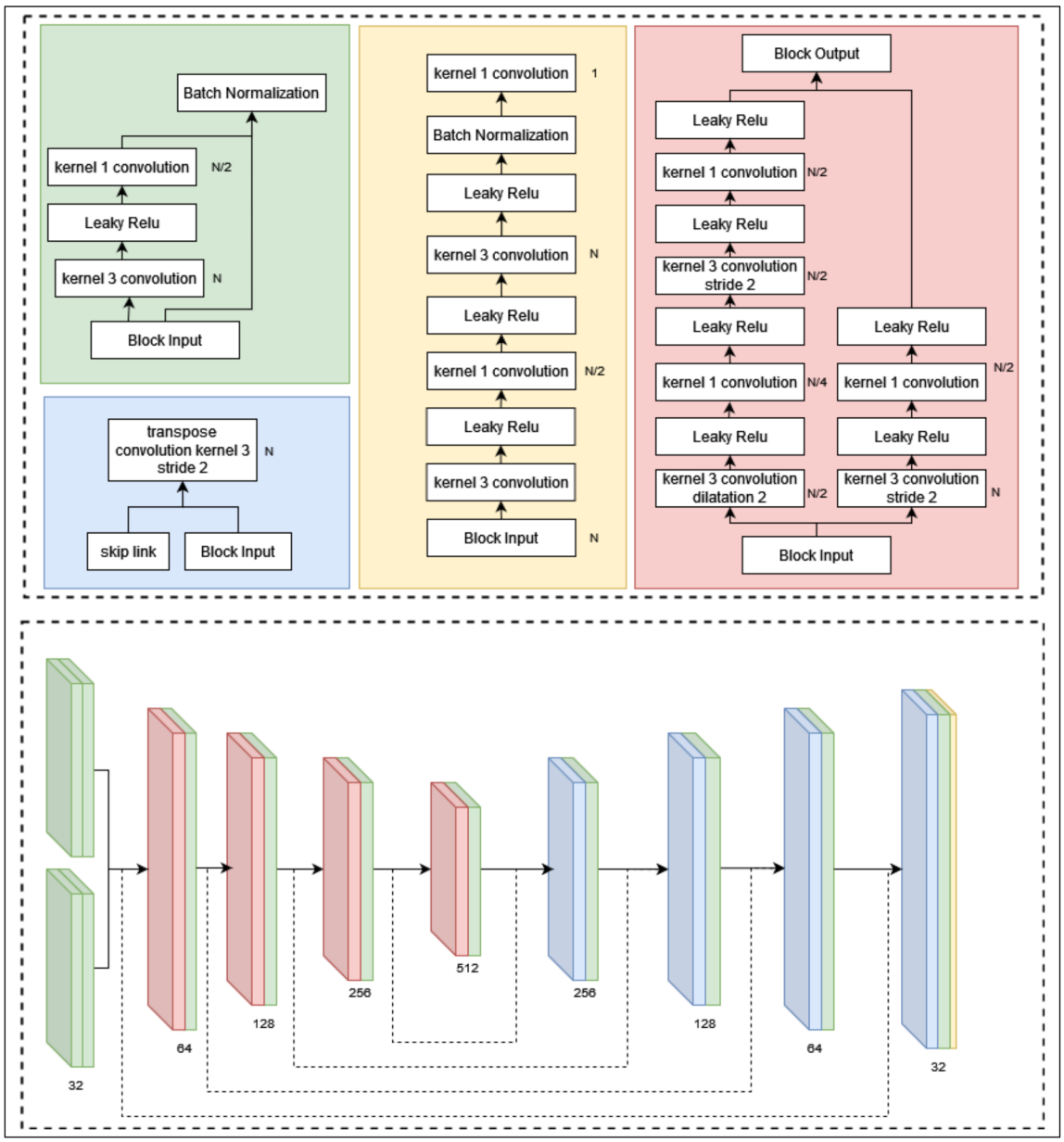

FIGURE 2.1. SI-QSM architecture.

The architecture has two input channels, the phase and a binary mask of the ROI. They are concatenated at the entrance of the encoder. The encoding layers include different parallel filters(Szegedy et al., 2014) and residual layers. The decoding part includes transposed convolutions and residual layers. To achieve faster reconstructions and let the network to

learn how to down-sample and up-sample the data, the max pooling and up-sample operations of the network were changed to stride 2 in the convolutional layers and the transpose convolutional layers.

In the convolutional layers we replaced the kernels of size 5 (proposed in the Inception Net architecture (Szegedy et al., 2014)), by dilated kernels of size 3. This way, the network can learn different features in the same layer and use less resources. All convolutions are initialized with the TensorFlow random seed 1024. We selected Leaky Relu as the activation function to be able to propagate the localization of scaled values of negative input voxels.

Using residual layers, a parallel layer paradigm and kernels of different sizes allow us to better propagate morphological patterns, to get different layer contexts and therefore, to get a nearly scale-invariant network for QSM reconstruction.

2.0.2. Data generation

Bollmann et al. (Bollmann et al., 2019) showed that a CNN-based QSM reconstruction network can be trained using a susceptibility distribution made of a collection of simple geometric structures (i.e., spheres and parallelepipeds) as ground truth, and computing the acquired magnetization via a discrete convolution with the dipole kernel. This strategy has been also replicated in subsequent studies (Li et al., 2021).

Instead of using discrete convolutions, we propose to use analytic solutions, since they produce more accurate susceptibility interfaces than numeric simulations (Salomir et al., 2003), and therefore reduce blurring or other scale-related problems. Analytic expressions for the magnetization of spheres and infinite cylinders of constant susceptibilities (χ) are well-known (Salomir et al., 2003; Cheng, Hsieh, Neelavalli, & Haacke, 2009; Brown,

Cheng, Haacke, Thompson, & Venkatesan, 1999). The magnetization produced by a sphere is given by:

$$B^{sphere}(x,y,z) = \begin{cases} B_0(1-\frac{2}{3}\chi_{out})(r^3\frac{\chi-\chi_{out}}{3+\chi-\chi_{out}})(\frac{2z^2-x^2-y^2}{(x^2+y^2+z^2)^{5/2}}), & \text{outside the sphere} \\ 0, & \text{inside the sphere} \end{cases} \tag{2.1}$$

where $B(x,x,z)$ is the magnetic induction at a given Cartesian coordinate (x,y,z), χ_{out} is the susceptibility outside the object, B_0 is the main magnetic field and r is the sphere radius.

For the infinite cylinder (of radius r), we exploit the symmetry of the problem by using tilted cylindrical coordinates and ignoring the polar angle:

$$B^{cylinder}(\rho,\psi) = \begin{cases} -B_0\frac{(\chi-\chi_{out})r^2}{2\rho}cos(2\psi)sin^2(\theta), & \text{outside the cylinder} \\ -B_0\frac{(\chi-\chi_{out})}{6}(3cos^2(\theta)-1), & \text{inside the cylinder} \end{cases} \tag{2.2}$$

where ρ is the perpendicular distance from a point to the central axis of the cylinder, ψ is the azimuth angle, and θ is the angle between the cylinder's axis and the main field direction (z).

Being our analytical forward model a linear operator, we can add multiple spheres and cylinders to build complex geometric figures (Milovic, Acosta-Cabronero, et al., 2018). For the training process, the susceptibility maps were used as output, whereas the magnetization field maps were used as input (Figure 2.2). We considered as random values: the number of spheres, the number of cylinders, the constant susceptibility inside each sphere or cylinder, the radius of each sphere or cylinder, the location of each sphere or cylinder and the cylinder orientation. For each example of the training dataset, we limited to 0.01 ppm the absolute value of the susceptibility of each sphere and each cylinders, we set to 0 the value of χ_{out},

and the maximum number of cylinders and spheres was set to 32 and 128, respectively. The field of view (FOV) of the training data was 48x48x48 voxels. As an augmentation step, we added Gaussian noise to the magnetization, with zero mean and standard deviation between 1×10^{-5} and 1×10^{-3} (constant for each data example).

2.0.3. Model training

The training was done with an Nvidia Titan RTX GPU, using Tensorflow Estimators, batch size 12, ADAM optimizer (Kingma & Ba, 2014), learning rate 1.5×10^{-4}, default beta parameters and the following loss function:

$$Loss = \frac{\alpha}{N} \sum |y - y'|^2 + \frac{\beta}{N} \sum |y - y'| + \frac{\gamma}{N} \sum |\nabla y'| \tag{2.3}$$

where y and y' are the reference and the prediction of the network, respectively, N is the number of image voxels and $\alpha = 1$, $\beta = 1 \times 10^{-4}$ and $\gamma = 1$ are the weights applied to each term in the loss function. This loss was designed to follow the optimization structure behind a successful iterative approach such as (Lambert, Tejos, Langkammer, & Milovic, 2022), which combines the L2-norm, L1-norm and total variation in its optimizing functionals.

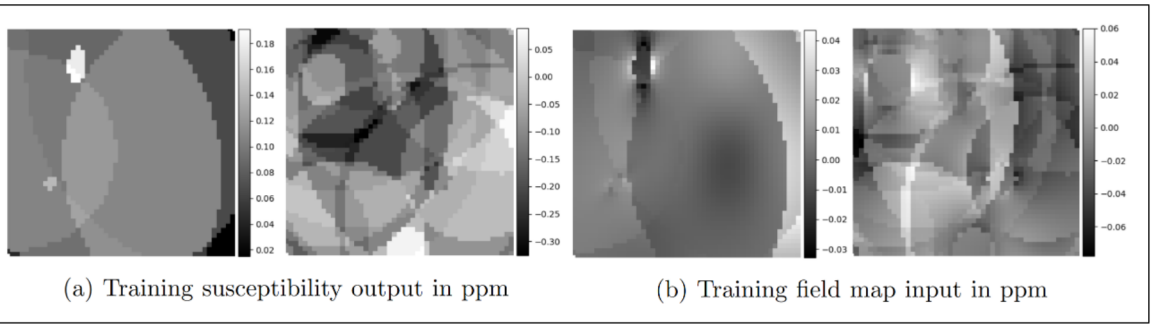

(a) Training susceptibility output in ppm (b) Training field map input in ppm

FIGURE 2.2. Generated training data with inputs and expected outputs.

The model was trained for 12 hours considering 5 epochs with 65.536 examples in the dataset. The model loss converged after 1 hour of training and the subsequent time window

was used to fine tune the model. After training, the model was optimized to half mixed precision inference.

2.0.4. Experiments

We compared our proposed method against iterative and alternative CNN-based approaches (DeepQSM (Bollmann et al., 2019) and QSMnet+ (Jung, Yoon, et al., 2020)). We used default weights or the pre-trained network provided by the authors. Specifically, the authors of QSMnet+ trained their network with 64x64x64-voxel patches obtained from COSMOS images (T. Liu, Spincemaille, De Rochefort, Kressler, & Wang, 2009) with a voxel size of 1 x 1 x 1mm^3, with overlaps of 66% (Yoon et al., 2018). The authors of DeepQSM trained their network using 48x48x48-voxel synthetic images.

2.0.4.1. Scale invariance

To test the ability of our network to reconstruct susceptibility maps at different spatial scales, we used a piece-wise constant susceptibility phantom (Wisnieff et al., 2013; Milovic, Bilgic, Zhao, Acosta-Cabronero, & Tejos, 2018). This phantom was reconstructed at four different scales. First, we zero-padded it from the original size 256x256x98 to 256x256x256 voxels. We downsampled this image to 128x128x128, 96x96x96, and 64x64x64 voxels. We forward simulated the magnetization by convolving with the dipole kernel. We added Gaussian noise with signal-to-noise ratio (SNR) = 100 to the simulate the final field maps. We measured the Root Mean Squared Error (RMSE) of each reconstruction and compared performances with DeepQSM and QSMnet+.

2.0.4.2. QSM Reconstruction Challenge data

The 2019 QSM Reconstruction Challenge (RC2) used a 7T MP2RAGEME (Caan et al., 2019) acquisition to build two in silico datasets (Sim1 and Sim2) (J. P. Marques et al., 2021). Each dataset includes a simulated multi-echo GRE acquisition, from which the local field map was estimated using a nonlinear fit (T. Liu et al., 2013). We also used the supplied field map, obtained from averaging phase differences (Bilgic et al., 2021). Both datasets have a FOV of 164x205x205 voxels, but each of them has a different contrast between grey

and white matter structures. Sim2 also includes a strong calcification. For the challenge, submitted reconstructions were analyzed using the global RMSE and local RMSE at different ROIs, along with metrics focused on the accuracy of the reconstructed susceptibility at the calcification and its surrounding tissues. We measured the performance of SI-QSM using the script provided by the challenge and compared our metric scores with those obtained by submitted approaches using Deep Learning algorithms (Bilgic et al., 2021). We also compared our approach with metric scores obtained by a Total Variation-regularized iterative solver (FANSI) (Milovic, Bilgic, et al., 2018), which was the top-scoring RMSE submitted approach for Stage 2, and a non-regularized early-stopped nonlinear iterative solver (NDI) (Polak et al., 2020). In this experiment we compared our method with QSMnet (Yoon et al., 2018), instead of QSMnet+, since the RC2 did not report results for the latter algorithm.

2.0.4.3. In vivo data

We reconstructed an in vivo data set of a healthy volunteer, acquired with a Turbo GRE sequence in a 3T Philips Ingenia scanner, with the following acquisition parameters: voxel size 0.59x0.59x1 mm, 5 echoes, TR/TE = 44/7.2 ms, echo spacing 6.2 ms, bandwidth of 550.5 Hz, FOV 352x352x160 voxels and a flip angle of 17 degrees. We performed a Laplacian phase unwrapping (Schofield & Zhu, 2003). Background field removal was performed by a two-step approach (Milovic et al., 2019; Acosta-Cabronero et al., 2018) using LBV (Zhou, Liu, Spincemaille, & Wang, 2014) and VSHARP (Özbay et al., 2017). We applied a bilinear interpolation to get a dataset with isotropic resolution.

We reconstructed a second in vivo acquisition (same scanner, acquisition parameters and interpolation) of a volunteer with a calcification. For this example, we applied SEGUE (Karsa & Shmueli, 2019) for phase unwrapping and PDF (T. Liu, Khalidov, et al., 2011) for background field removal. Background field residuals were removed using the harmonic phase estimation obtained with the Weak-harmonic QSM method (WH-TV) (Milovic et

al., 2019).

For both reconstructions we compared our proposed method with four state-of-the-art algorithms: FANSI, NDI, QSMnet+ and DeepQSM.

The acquisitions were performed after an informed consent was signed by the volunteers and under the approval of the Institutional Ethics Committee.

3. RESULTS

3.0.1. Scale invariance

As shown in Table 3.1, for small scales, SI-QSM and QSMnet+ obtained similar RMSE scores, outperforming DeepQSM. Whereas QSMnet+ maintained its performance for large scales, our approach reduced the reconstructed errors. Errors produced by DeepQSM were dominated by susceptibility overestimations (Figure 3.1), although in some regions there were also some underestimated susceptibilities (e.g., close to the corpus callosum). Less significant, but also visible, were some streaking artifacts (shown at the difference maps at Figure 3.1). Errors produced by QSMnet+ also showed an oscillatory pattern with underestimated and overestimated areas, although less severe than that in DeepQSM. Whereas at small scales reconstructions tended to be blurred, at large scales smoothing problems disappeared, but some streaking artifacts became visible. SI-QSM also showed some blurring at small scales, which tended to disappear at larger scales, but without creating oscillatory patterns or significant streaking artifacts, and constantly reducing the magnitude of the errors.

TABLE 3.1. RMSE results for the CNN-based QSM reconstruction method in ppm.

	FOV Scale			
	64^3	96^3	128^3	256^3
DeepQSM	3.27×10^{-3}	3.03×10^{-3}	2.94×10^{-3}	3.14×10^{-3}
QSMnet+	2.39×10^{-3}	2.10×10^{-3}	2.22×10^{-3}	2.22×10^{-3}
SI-QSM	2.42×10^{-3}	2.21×10^{-3}	2.02×10^{-3}	1.74×10^{-3}

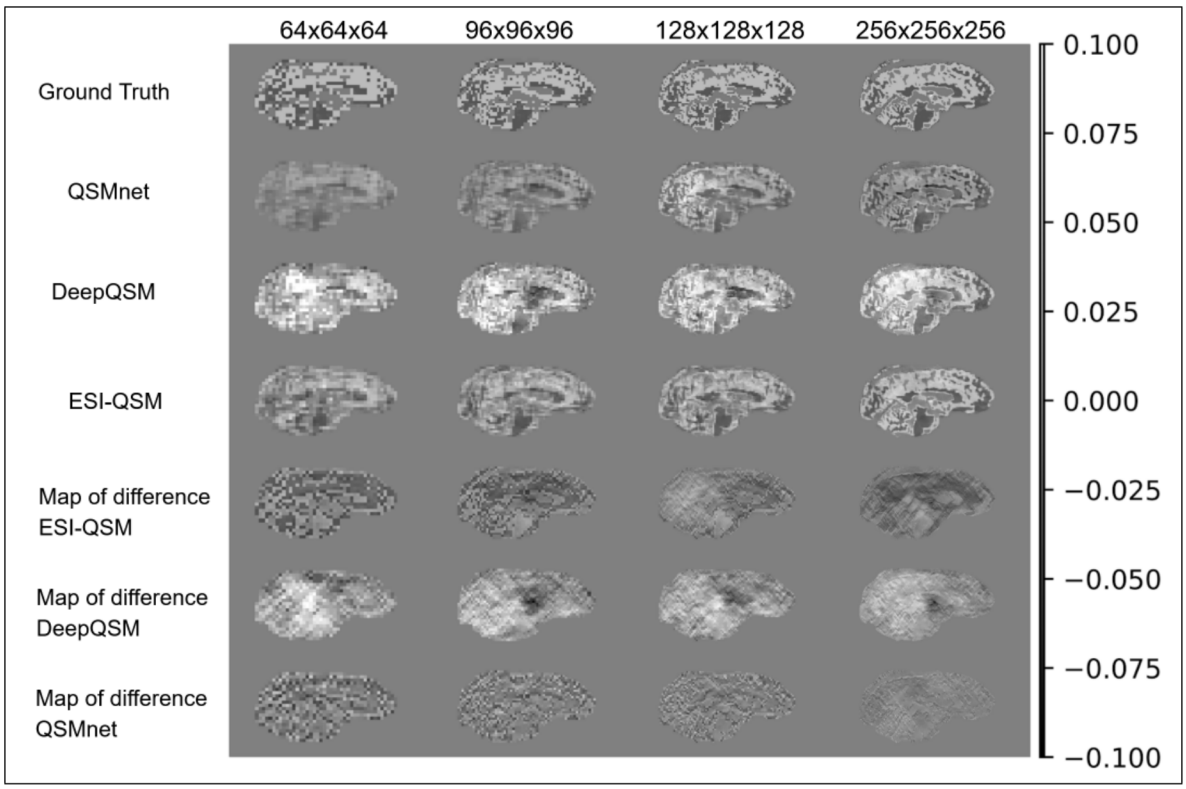

FIGURE 3.1. Comparison of CNN-based QSM reconstructions at different FOV scales. All susceptibility values are in ppm.

3.0.2. QSM Reconstruction Challenge data

Figure 3.2 shows the reconstructions for the Sim2 RC2 dataset and Figure 3.3 shows the respective differences with the ground truth. Note that we are including the openly available FANSI, DeepQSM and QSMnet reconstructions submitted to the Stage 2 of the challenge (Bilgic et al., 2021). The NDI reconstruction was performed by running 200 gradient-descent iterations, and with a Tikhonov weight of 1×10^{-6}. Evaluation metrics are shown in Table 3.2.

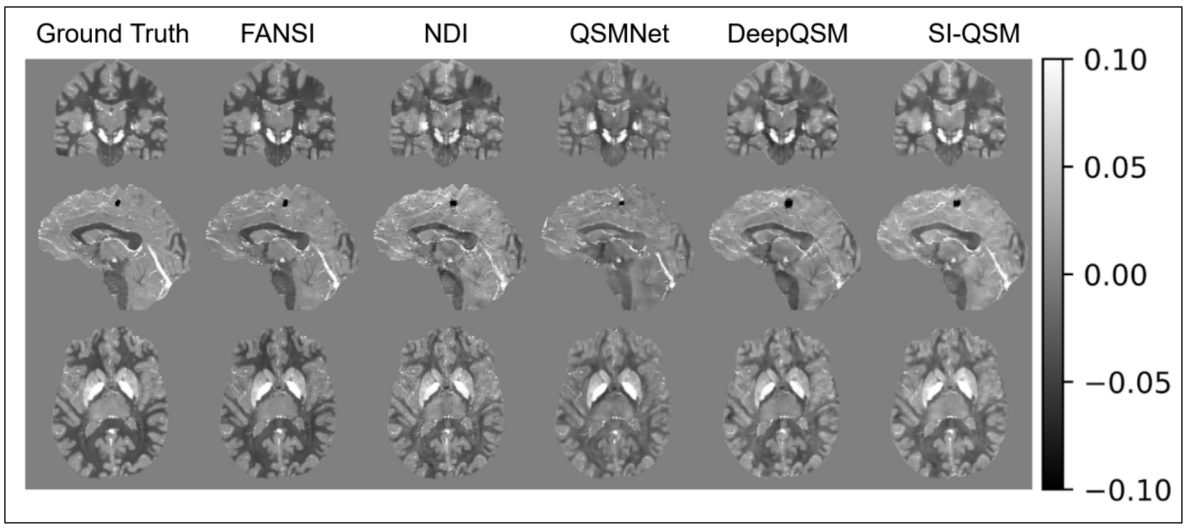

FIGURE 3.2. QSM reconstructions (in ppm) obtained by different methods using the RC2 data.

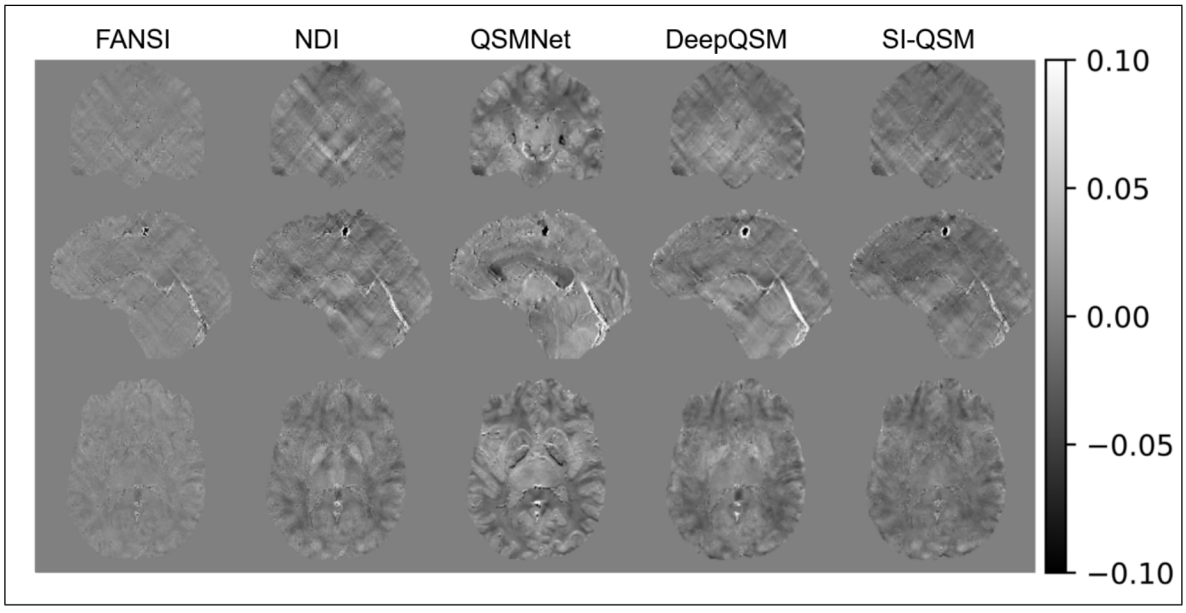

FIGURE 3.3. Difference maps between the ground truth and the compared reconstruction approaches. All results are in ppm.

TABLE 3.2. Metric scores obtained by different reconstruction methods using the RC2 data.

	FANSI	NDI	DeepQSM	QSMnet	SI-QSM
nrmse	28.85	51.15	58.28	63.18	49.13
nrmse_detrend	30.16	54.73	71.77	82.006	51.89
nrmse_detrend_Tissue	36.92	59.32	90.37	107.64	59.35
nrmse_detrend_Blood	62.92	71.46	132.41	153.83	68.43
nrmse_detrend_DGM	19.92	42.22	32.93	39.42	28.07
DeviationFrom LinearSlope	0.014	0.204	0.159	0.062	0.087
CalcStreak	0.013	0.096	0.093	0.10	0.075
DeviationFrom CalcMoment	5.75	27.24	36.46	45.51	21.28

In terms of structural details, FANSI seems to have the best performance, followed by SI-QSM. QSMnet, DeepQSM and NDI generated blurred susceptibility maps, which fail to reconstruct accurately small structures such as the straight sinus (Figure 3.2). This becomes more evident in the difference maps (Figure 3.3). Both, NDI and our solution produced similar results for medium and large-scale features, however our method showed a better management of high-frequency noise. All methods had problems to reconstruct accurately the calcification, since all of them producing a larger lesion, with an incorrect susceptibility value. A similar behaviour can be observed analyzing the quantitative metrics (Table 3.2). SI-QSM outperformed DeepQSM, QSMnet and NDI, being the second best after FANSI.

3.0.3. In vivo data

QSM reconstructions of in vivo data from the healthy volunteer are shown in Figure 3.4 and QSM reconstructions of the subject with a strong calcification are shown in Figure 3.5. QSMnet+ and DeepQSM produced reconstructions with low contrast and also some

attenuation is visible in deep brain structures. DeepQSM also produced blurred reconstructions. Contrast is substantially increased in FANSI, NDI and SI-QSM reconstructions. These methods also showed good definition of small structures, although NDI produced some streaking artifacts and noisy results. These streaking artifacts are more evident when emanating from high-contrast features, as for the calcifications. All compared methods seem to be sensitive to background field residuals, as shown in Figure 3.4. Finally, each method produced a slightly different result for the calcification (Figures 3.5 and 3.6).

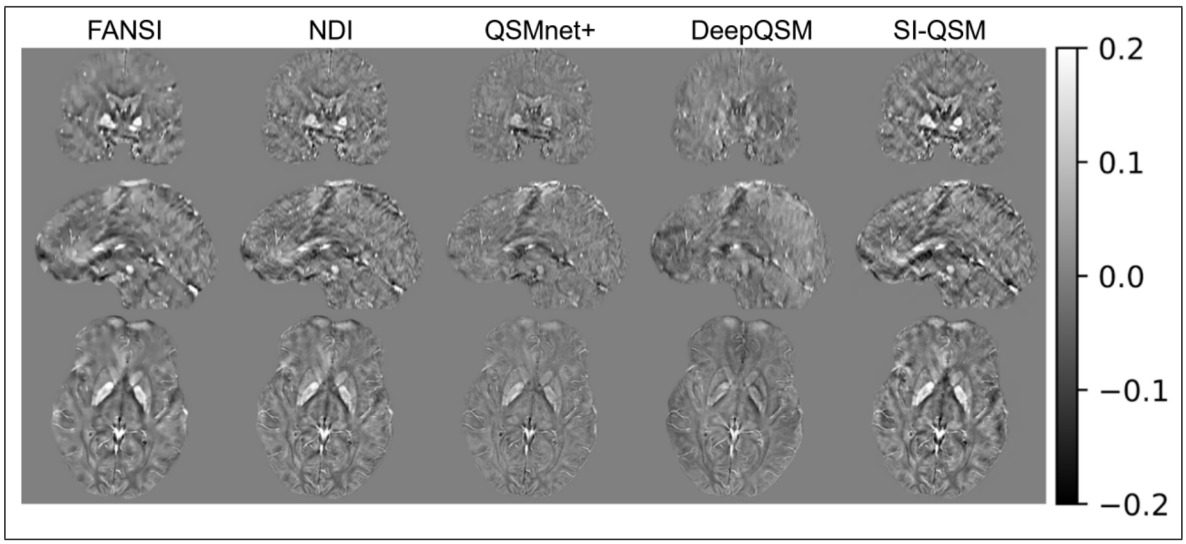

FIGURE 3.4. QSM reconstructions (in ppm) of a healthy volunteer.

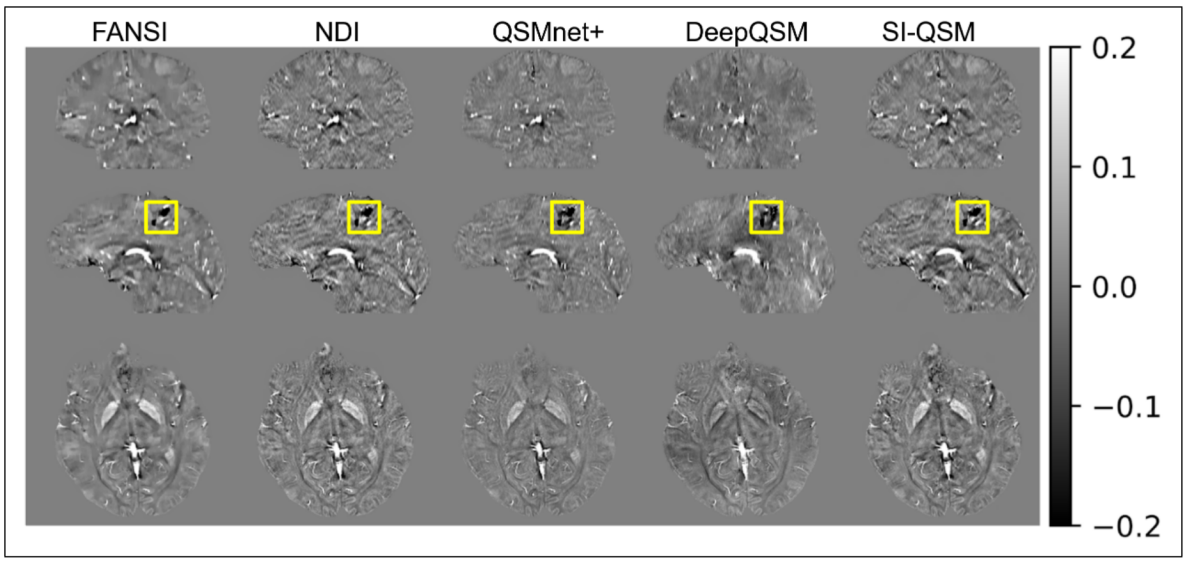

FIGURE 3.5. QSM reconstructions (in ppm) of a subject with a calcification.

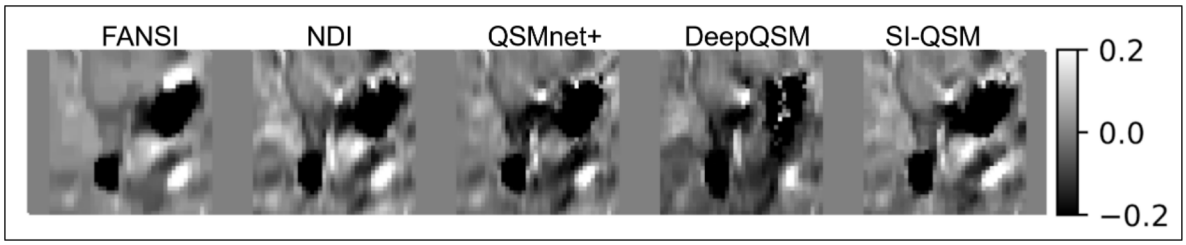

FIGURE 3.6. QSM reconstructions (in ppm) of a subject with a calcification. Magnified view of a ROI around the calcification.

4. DISCUSSION

Traditional Deep Leaning-based QSM approaches show accurate reconstructions for structures with similar sizes as those included in the training process. However, reconstruction quality gets worse for structures of other sizes. This might be observed for QSMnet+, which gave attenuated results for very large deep brain structures. Such structures are larger than the training patches. Although DeepQSM has a different training strategy, the results show a similar pattern. The algorithm failed to reconstruct structures that are larger than those included in the training set. Both algorithms also failed to reconstruct small structures with large susceptibility values (e.g., straight sinus). Our SI-QSM was able to keep a good reconstruction performance across different scales. In fact, for large FOV scales, all metrics tended to improve and errors are characterized by high-frequency components only.

This behaviour may be explained by the use of training data based on an analytical model, the incorporation of residual layers and different types of kernels and the use of a loss function that balance L1-norm, L2-norm and a total variation regularization. Further investigations need to be done to determine how each of these factors affect the QSM reconstructions. This might be done for example with layer analysis, pruning or changing the training dataset and changing the loss function.

Visually, our reconstructions are similar to those achieved by NDI. In essence, NDI uses the iterations as an implicit regularization and the Tikhonov weight acts only as a means to stabilize those iterations (Polak et al., 2020). This seems to be an effective strategy to reduce noise and streaking artifacts. Similarly, our network was very effective in learning the underlying physical inverse problem, without producing noise amplification or streaking artifacts.

SI-QSM performed well on the in silico datasets presented at the 2019 QSM Reconstruction Challenge, outperforming DeepQSM and QSMnet. If we would consider the

entire list of submitted deep learning-based approaches, SI-QSM would obtain the second place in the RMSE category. We expect that the computed metrics might be improved by fine-tuning our model to the susceptibility distribution of the RC2 data. However, this might not guarantee a good overall performance and might produce over-fitting. This is also something that requires a further analysis.

In its current form, our model requires local field maps with isotropic resolution. Reconstructing anisotropic datasets leads to ghosting and other artifacts. This might be explained by the fact that our network was trained only with isotropic voxels. To deal with this limitation we used bilineal interpolations to achieve isotropic in vivo data. As a future work, we might study whether including datasets with anisotropic resolutions into the training process would capture the underlying physics involved in this inverse problem.

Reconstructing accurately structures with abrupt susceptibility changes (e.g., large veins and calcifications) seems to be a big challenge for all QSM approaches, iterative and deep learning-based. The reconstructed susceptibility values of those structures, and sometimes those of the surrounding structures, seems to be biased. Including such structures into the training datasets might improve these results, but this is something that needs to be further investigated.

Reconstruction algorithms present significant differences in terms of speed. Whereas ES-QSM took typically 15 to 30 seconds to reconstruct in vivo datasets, NDI took between 1 to 3 minutes. This difference is even larger for FANSI, which took 15 to 20 minutes. These times do not consider that iterative methods need fine-tuning weighting parameters, therefore the reported time must be multiplied by the number of attempts needed for setting those parameters.

Recent developments have shown that a single network could be trained to perform simultaneously both, the background field removal and the dipole inversion steps (J. Liu & Koch, 2019). We are also considering this as a future area of research.

5. CONCLUSIONS

Although deep learning-based approaches have significantly contributed to the state of the art in QSM, they still produce significant errors when there is a mismatch in spatial scale between the training dataset and the reconstructed susceptibility maps.

We here proposed SI-QSM, a deep learning-based algorithm for QSM reconstruction. We innovated in both, training and architectures aspects. For training, we proposed the use of an analytical model to create our training data set and also a loss function that integrates L1-norm, L2-norm and a total variation regularization. In terms of architecture, our U-net-based structure combines residual layers, different types of kernels with different sizes. The resulting network was able to overcome successfully those scale-related problems. Indeed, training at a particular spatial scale allowed accurate reconstructions of susceptibility maps of different scales, without producing blurred structures, biased susceptibilities and with good control over noise, streaking or similar artifacts.

REFERENCES

Acosta-Cabronero, J., Cardenas-Blanco, A., Betts, M. J., Butryn, M., Valdes-Herrera, J. P., Galazky, I., & Nestor, P. J. (2017). The whole-brain pattern of magnetic susceptibility perturbations in Parkinson's disease. *Brain: a journal of neurology*, *140*(1), 118-131.

Acosta-Cabronero, J., Milovic, C., Mattern, H., Tejos, C., Speck, O., & Callaghan, M. F. (2018). A robust multi-scale approach to quantitative susceptibility mapping. *NeuroImage*, *183*, 7-24.

Acosta-Cabronero, J., Williams, G. B., Cardenas-Blanco, A., Arnold, R. J., Lupson, V., & Nestor, P. J. (2013). In Vivo Quantitative Susceptibility Mapping (QSM) in Alzheimer's Disease. *PLoS one*, *8*(11), e81093.

Bilgic, B., Chatnuntawech, I., Langkammer, C., & Setsompop, K. (2015). Sparse methods for Quantitative Susceptibility Mapping. In *Wavelets and sparsity xvi* (pp. 237 – 246). SPIE.

Bilgic, B., Langkammer, C., Marques, J. P., Meineke, J., Milovic, C., & Schweser, F. (2021). QSM reconstruction challenge 2.0: Design and report of results. *Magnetic Resonance in Medicine*, *86*, 1241-1255.

Bollmann, S., Rasmussen, K. G. B., Kristensen, M., Blendal, R. G., Østergaard, L. R., Plocharski, M., ... Barth, M. (2019). DeepQSM - using deep learning to solve the dipole inversion for quantitative susceptibility mapping. *NeuroImage*, *195*, 373-383.

Brown, R. W., Cheng, Y.-C. N., Haacke, E. M., Thompson, M. R., & Venkatesan, R. (1999). *Journal of Magnetic Resonance Imaging : Physical Principles and Sequence Design*. New York: Wiley. Print.

Caan, M. W., Bazin, P. L., Marques, J. P., de Hollander, G., Dumoulin, S. O., & van der Zwaag, W. (2019). MP2RAGEME: T 1 , T 2* , and QSM mapping in one sequence at 7 tesla. *Human Brain Mapping*, *40*, 1786-1798.

Chen, Y., Jakary, A., Avadiappan, S., Hess, C. P., & Lupo, J. M. (2020). QSMGAN: Improved Quantitative Susceptibility Mapping using 3D Generative Adversarial Networks with increased receptive field. *NeuroImage*, *207*, 116389.

Cheng, Y.-C. N., Hsieh, C.-Y., Neelavalli, J., & Haacke, E. M. (2009). Quantifying effective magnetic moments of narrow cylindrical objects in MRI. *Physics in Medicine and Biology*, *54*(22), 7025–7044.

Duyn, J. H., Gelderen, P. V., Li, T. Q., Zwart, J. A. D., Koretsky, A. P., & Fukunaga, M. (2007). High-field MRI of brain cortical substructure based on signal phase. *Proceedings of the National Academy of Sciences*, *104*, 11796-11801.

Feng, R., Zhao, J., Wang, H., Yang, B., Feng, J., Shi, Y., ... Wei, H. (2021). MoDL-QSM: Model-based deep learning for quantitative susceptibility mapping. *NeuroImage*, *240*, 118376.

Gao, Y., Zhu, X., Moffat, B. A., Glarin, R., Wilman, A. H., Pike, G. B., ... Sun, H. (2021). xQSM: quantitative susceptibility mapping with octave convolutional and noise-regularized neural networks. *NMR in Biomedicine*, *34*, e4461.

Goodfellow, I. J., Pouget-Abadie, J., Mirza, M., Xu, B., Warde-Farley, D., Ozair, S., ... Bengio, Y. (2014). Generative Adversarial Networks. In *Advances in neural information processing systems* (pp. 2672–2680).

Haacke, E. M., Liu, S., Buch, S., Zheng, W., Wu, D., & Ye, Y. (2015). Quantitative susceptibility mapping: current status and future directions. *Journal of Magnetic Resonance Imaging*, *33*, 1-25.

Haacke, M., Tang, J., Neelavalli, J., & Cheng, Y.-C. (2010). SWIM: Susceptibility Mapping as a Means to Visualize Veins and Quantify Oxygen Saturation. *Journal of Magnetic Resonance Imaging*, *32*, 663-76.

Hansen, P. C. (1992). Analysis of Discrete Ill-Posed Problems by Means of the L-Curve. *SIAM Rev. Soc. Ind. Appl. Math.*, *34*, 561–580.

Jung, W., Bollmann, S., & Lee, J. (2020). Overview of quantitative susceptibility mapping using deep learning: Current status, challenges and opportunities. *NMR in Biomedicine*, *35*, e4292.

Jung, W., Yoon, J., Ji, S., Choi, J. Y., Kim, J. M., Nam, Y., ... Lee, J. (2020). Exploring linearity of deep neural network trained QSM: QSMnet+. *NeuroImage*, *211*, 116619.

Karsa, A., & Shmueli, K. (2019). SEGUE: A Speedy Region-Growing Algorithm for Unwrapping Estimated Phase. *IEEE Transactions on Medical Imaging*, *38*, 1347-1357.

Kingma, D. P., & Ba, J. (2014). Adam: A Method for Stochastic Optimization.

Lambert, M., Tejos, C., Langkammer, C., & Milovic, C. (2022). Hybrid data fidelity term approach for quantitative susceptibility mapping. *Magnetic Resonance in Medicine*, 1-11.

Langkammer, C., Pirpamer, L., Seiler, S., Deistung, A., Schweser, F., Franthal, S., ... Schwingenschuh, P. (2016). Quantitative Susceptibility Mapping in Parkinson's Disease. *PLoS one*, *11*, 1-13.

Li, Z., Li, J., Wang, C., Lu, Z., Wang, J., He, H., & Shi, J. (2021). Meta-Learning Based Interactively Connected Clique U-Net for Quantitative Susceptibility Mapping. *IEEE Transactions on Computational Imaging*, *7*, 1385-1399.

Liu, J., & Koch, K. M. (2019). Deep Quantitative Susceptibility Mapping for Background Field Removal and Total Field Inversion.

Liu, T., Khalidov, I., de Rochefort, L., Spincemaille, P., Liu, J., Tsiouris, A. J., & Wang, Y. (2011). A novel background field removal method for MRI using projection onto dipole fields (PDF). *NMR in Biomedicine*, *24*, 1129-1136.

Liu, T., Liu, J., de Rochefort, L., Spincemaille, P., Khalidov, I., Ledoux, J. R., & Wang, Y. (2011). Morphology enabled dipole inversion (MEDI) from a single-angle acquisition: comparison with COSMOS in human brain imaging. *Magnetic Resonance in Medicine*, *66*(3), 777–783.

Liu, T., Spincemaille, P., De Rochefort, L., Kressler, B., & Wang, Y. (2009). Calculation of susceptibility through multiple orientation sampling (COSMOS): a method for conditioning the inverse problem from measured magnetic field map to susceptibility source image in MRI. *Magnetic Resonance in Medicine*, *61*, 196–204.

Liu, T., Surapaneni, K., Lou, M., Cheng, L., Spincemaille, P., & Wang, Y. (2012). Cerebral Microbleeds: Burden Assessment by Using Quantitative Susceptibility Mapping. *Radiology*, *262*, 269-278.

Liu, T., Wisnieff, C., Lou, M., Chen, W., Spincemaille, P., & Wang, Y. (2013). Nonlinear formulation of the magnetic field to source relationship for robust quantitative susceptibility mapping. *Magnetic Resonance in Medicine*, *69*, 467–476.

Marques, J., & Bowtell, R. (2005). Application of a Fourier-based method for rapid calculation of field inhomogeneity due to spatial variation of magnetic susceptibility. *Concepts in Magnetic Resonance Part B: Magnetic Resonance Engineering*, *25B*, 65–78.

Marques, J. P., Meineke, J., Milovic, C., Bilgic, B., Chan, K. S., Hedouin, R., ... Schweser, F. (2021). QSM reconstruction challenge 2.0: A realistic in silico head

phantom for MRI data simulation and evaluation of susceptibility mapping procedures. *Magnetic Resonance in Medicine*, *86*, 526-542.

Milovic, C., Acosta-Cabronero, J., Pinto, J. M., Mattern, H., Andia, M., Uribe, S., & Tejos, C. (2018). A new discrete dipole kernel for quantitative susceptibility mapping. *Magnetic Resonance Imaging*, *51*, 7-13.

Milovic, C., Bilgic, B., Zhao, B., Acosta-Cabronero, J., & Tejos, C. (2018). Fast nonlinear susceptibility inversion with variational regularization. *Magnetic Resonance in Medicine*, *80*, 814-821.

Milovic, C., Bilgic, B., Zhao, B., Langkammer, C., Tejos, C., & Acosta-Cabronero, J. (2019). Weak-harmonic regularization for quantitative susceptibility mapping. *Magnetic Resonance in Medicine*, *81*, 1399-1411.

Milovic, C., Prieto, C., Bilgic, B., Uribe, S., Acosta-Cabronero, J., Irarrazaval, P., & Tejos, C. (2021). Comparison of parameter optimization methods for quantitative susceptibility mapping. *Magnetic Resonance in Medicine*, *85*, 480-494.

Oh, G., Bae, H., Ahn, H.-S., Park, S.-H., & Ye, J. C. (2020). CycleQSM: Unsupervised QSM Deep Learning using Physics-Informed CycleGAN.

Polak, D., Chatnuntawech, I., Yoon, J., Iyer, S. S., Milovic, C., Lee, J., ... Bilgic, B. (2020). Nonlinear dipole inversion (NDI) enables robust quantitative susceptibility mapping (QSM). *NMR in Biomedicine*, *33*, e4271.

Robinson, S. D., Bredies, K., Khabipova, D., Dymerska, B., Marques, J. P., & Schweser, F. (2017). An illustrated comparison of processing methods for MR phase imaging and QSM: combining array coil signals and phase unwrapping. *NMR in Biomedicine*, *30*, e3601.

Ronneberger, O., Fischer, P., & Brox, T. (2015). U-Net: Convolutional Networks for Biomedical Image Segmentation. In *Medical image computing and computer-assisted intervention – miccai* (pp. 234–241).

Salomir, R., Senneville, B. D. D., & Moonen, C. T. (2003). A fast calculation method for magnetic field inhomogeneity due to an arbitrary distribution of bulk susceptibility. *Concepts in Magnetic Resonance Part B: Magnetic Resonance Engineering*, *19B*, 26-34.

Schofield, M., & Zhu, Y. (2003). Fast phase unwrappng algorithm for interferometric applications. *Optics letters*, *28*, 1194-6.

Schweser, F., Robinson, S. D., de Rochefort, L., Li, W., & Bredies, K. (2017). An illustrated comparison of processing methods for phase MRI and QSM: removal of background field contributions from sources outside the region of interest. *NMR in Biomedicine*, *30*, e3604.

Shmueli, K., Zwart, J. A. D., Gelderen, P. V., Li, T. Q., Dodd, S. J., & Duyn, J. H. (2009). Magnetic susceptibility mapping of brain tissue in vivo using MRI phase data. *Magnetic Resonance in Medicine*, *62*, 1510-1522.

Szegedy, C., Liu, W., Jia, Y., Sermanet, P., Reed, S., Anguelov, D., ... Rabinovich, A. (2014). Going Deeper with Convolutions.

Wang, Y., & Liu, T. (2015). Quantitative susceptibility mapping (QSM): Decoding MRI data for a tissue magnetic biomarker. *Magnetic Resonance in Medicine*, *73*, 82-101.

Wharton, S., & Bowtell, R. (2010). Whole-brain susceptibility mapping at high field: a comparison of multiple- and single-orientation methods. *NeuroImage*, *53*, 515-525.

Wharton, S., Schäfer, A., & Bowtell, R. (2010). Susceptibility mapping in the human brain using threshold-based k-space division. *Magnetic Resonance in Medicine*, *63*, 1292–1304.

Wisnieff, C., Liu, T., Spincemaille, P., Wang, S., Zhou, D., & Wang, Y. (2013). Magnetic susceptibility anisotropy: cylindrical symmetry from macroscopically ordered anisotropic molecules and accuracy of mri measurements using few orientations. *NeuroImage*, *70*, 363-376.

Yoon, J., Gong, E., Chatnuntawech, I., Bilgic, B., Lee, J., Jung, W., ... Lee, J. (2018). Quantitative susceptibility mapping using deep neural network: QSMnet. *NeuroImage*, *179*, 199-206.

Zhang, Y., Gauthier, S. A., Gupta, A., Comunale, J., Chiang, G. C.-Y., Zhou, D., ... Wang, Y. (2016). Longitudinal change in magnetic susceptibility of new enhanced multiple sclerosis (MS) lesions measured on serial quantitative susceptibility mapping (QSM). *Journal of Magnetic Resonance Imaging*, *44*, 426-432.

Zhou, D., Liu, T., Spincemaille, P., & Wang, Y. (2014). Background Field Removal by Solving the Laplacian Boundary Value Problem. *NMR in Biomedicine*, *27*, 312-319.

Özbay, P. S., Deistung, A., Feng, X., Nanz, D., Reichenbach, J. R., & Schweser, F. (2017). A comprehensive numerical analysis of background phase correction with V-SHARP. *NMR in Biomedicine*, *30*, e3550.